

# *The High-Resolution Coronal Imager (Hi-C)*

**Ken Kobayashi, Jonathan Cirtain,  
Amy R. Winebarger, Kelly Korreck,  
Leon Golub, Robert W. Walsh, Bart De  
Pontieu, Craig DeForest, et al.**

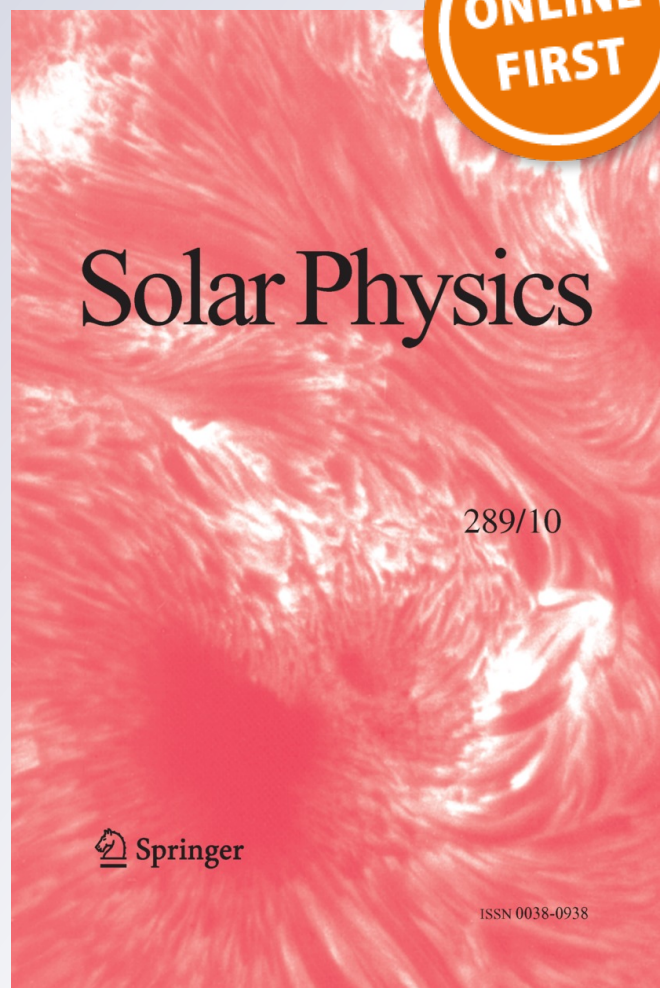
## **Solar Physics**

A Journal for Solar and Solar-Stellar  
Research and the Study of Solar  
Terrestrial Physics

ISSN 0038-0938

Sol Phys

DOI 10.1007/s11207-014-0544-4



**Your article is protected by copyright and all rights are held exclusively by Springer Science+Business Media Dordrecht (outside the USA). This e-offprint is for personal use only and shall not be self-archived in electronic repositories. If you wish to self-archive your article, please use the accepted manuscript version for posting on your own website. You may further deposit the accepted manuscript version in any repository, provided it is only made publicly available 12 months after official publication or later and provided acknowledgement is given to the original source of publication and a link is inserted to the published article on Springer's website. The link must be accompanied by the following text: "The final publication is available at [link.springer.com](http://link.springer.com)".**

## The *High-Resolution Coronal Imager* (Hi-C)

**Ken Kobayashi · Jonathan Cirtain · Amy R. Winebarger · Kelly Korreck · Leon Golub · Robert W. Walsh · Bart De Pontieu · Craig DeForest · Alan Title · Sergey Kuzin · Sabrina Savage · Dyana Beabout · Brent Beabout · William Podgorski · David Caldwell · Kenneth McCracken · Mark Ordway · Henry Bergner · Richard Gates · Sean McKillop · Peter Cheimets · Simon Platt · Nick Mitchell · David Windt**

Received: 11 June 2013 / Accepted: 25 April 2014  
© Springer Science+Business Media Dordrecht (outside the USA) 2014

**Abstract** The *High-Resolution Coronal Imager* (Hi-C) was flown on a NASA sounding rocket on 11 July 2012. The goal of the Hi-C mission was to obtain high-resolution ( $\approx 0.3 - 0.4''$ ), high-cadence ( $\approx 5$  seconds) images of a solar active region to investigate the dynamics of solar coronal structures at small spatial scales. The instrument consists of a

---

K. Kobayashi (✉)  
Center for Space Plasma and Aeronomic Research, The University of Alabama in Huntsville,  
320 Sparkman Dr., Huntsville, AL 35805, USA  
e-mail: [ken.kobayashi-1@nasa.gov](mailto:ken.kobayashi-1@nasa.gov)

*Present address:*  
K. Kobayashi  
NASA Marshall Space Flight Center, ZP 13, Huntsville, AL 35812, USA

J. Cirtain · A.R. Winebarger · S. Savage · D. Beabout · B. Beabout  
NASA Marshall Space Flight Center, ZP 13, Huntsville, AL 35812, USA

K. Korreck · L. Golub · W. Podgorski · D. Caldwell · K. McCracken · M. Ordway · H. Bergner ·  
R. Gates · S. McKillop · P. Cheimets  
Harvard-Smithsonian Center for Astrophysics, 60 Garden St., Cambridge, MA 02138, USA

R.W. Walsh · S. Platt · N. Mitchell  
University of Central Lancashire, Preston, Lancashire, UK, PR1 2HE

B. De Pontieu · A. Title  
Lockheed Martin Solar & Astrophysics Lab, 3251 Hanover St., Org. A0215, Bldg. 252, Palo Alto,  
CA 94304, USA

C. DeForest  
Southwest Research Institute, 1050 Walnut Street, Suite 300, Boulder, CO 80302, USA

S. Kuzin  
P.N. Lebedev Physical Institute of the Russian Academy of Sciences, Leninskii prospekt, 53, 119991,  
Moscow, Russia

D. Windt  
Reflective X-ray Optics, LLC, 1361 Amsterdam Ave., Suite 3B, New York, NY 10027, USA

normal-incidence telescope with the optics coated with multilayers to reflect a narrow wavelength range around 19.3 nm (including the Fe XII 19.5-nm spectral line) and a  $4096 \times 4096$  camera with a plate scale of  $0.1'' \text{ pixel}^{-1}$ . The target of the Hi-C rocket flight was Active Region 11520. Hi-C obtained 37 full-frame images and 86 partial-frame images during the rocket flight. Analysis of the Hi-C data indicates the corona is structured on scales smaller than currently resolved by existing satellite missions.

**Keywords** Solar corona · Solar instrumentation · Solar imaging · Extreme ultraviolet

## 1. Introduction

One of the key factors in improving our understanding of coronal physics has been the continued development of high-resolution imaging, particularly in the X-ray and EUV spectral regime. Beginning in the 1960s, direct on-disk imaging of the X-ray corona became available, leading to a clear understanding of the close connection between surface magnetic fields and X-ray emission (Vaiana *et al.*, 1973). The improved spatial resolution of the *Skylab* instruments (Zombeck *et al.*, 1978) led to the view that the corona is composed of loop-like structures representing isolated mini-atmospheres (Rosner, Tucker, and Vaiana, 1978). Improvements in spatial resolution with the *Yohkoh/Soft X-ray Telescope* (SXT) led to an acceptance of the role of magnetic reconnection in coronal dynamics (Tsuneta, 1996). Further improvement in coronal imaging was provided by normal-incidence EUV telescopes made possible by EUV multilayer coatings; this was pioneered by the *SOHO/EUV Imaging Telescope* (EIT: Delaboudinière *et al.*, 1995). The highest spatial resolution in images of the solar corona from a satellite mission was achieved with the *Transition Region and Coronal Explorer* (TRACE: Handy *et al.*, 1999). Analysis of those data led to a far more elaborate model of coronal structure and dynamics including three-dimensional-magnetic-field topologies defined by null points, separators and bald patches, and other topological features (Démoulin, 2005). There have been no additional improvements in spatial resolution of coronal images since the launch of TRACE in 1998; the *Atmospheric Imaging Assembly* (AIA: Lemen *et al.*, 2012) onboard the *Solar Dynamics Observatory* has more wavelengths and a larger field of view, but it has roughly the same resolution as TRACE ( $\approx 1.2''$ ).

The need to improve the spatial resolution of the observations is driven by the spatial scales that govern energy release in the corona. Complex photospheric driving can produce narrow current structures, possibly even current sheets, in a low-resistivity coronal field (Parker, 1972; van Ballegoijen, 1985). These structures persist in the presence of a uniform, small electrical resistivity since only slow Sweet–Parker magnetic reconnection is possible under these circumstances. Theoretical advances suggest that some localized anomalous resistivity must be triggered within the current sheets to produce fast Petschek reconnection capable of rapidly dissipating the current and releasing the stored magnetic energy. Reconnection localized in both space and time will produce slender tubes of reconnected flux (Linton and Longcope, 2006). These newly reconnected flux tubes will retract from the reconnection site at the local Alfvén speed, thereby rapidly releasing magnetic energy stored far outside the reconnection region itself. A corona heated in this way would be composed of numerous, discrete, bright loops, much as the actual corona is.

Although it is well beyond the reach of current instrumentation to resolve current sheets, meaning the interface region between entwined magnetic structures, the spatial scale of the heating determines the spatial scale of the structures. There is significant indication that strands, *i.e.* structures that have a similar temperature and density across their width, have a

transverse scale of a few hundred kilometers. A study of 20 loops observed with AIA and the *Extreme-ultraviolet Imaging Spectrometer* (EIS) onboard *Hinode* has found that observed loops at  $\approx 1.5$  MK can be explained as one to several strands with widths of 450–3000 km (Brooks, Warren, and Ugarte-Urra, 2012). Analysis of the footpoints of higher temperature ( $> 2$  MK) active-region core loops, or “moss,” observed with EIS has determined the filling factor of  $\approx 15\%$ , which equates to a scale size of roughly 300 km (Warren *et al.*, 2008). Additionally, some chromospheric features observed in the high-resolution ( $0.054'' \text{ pixel}^{-1}$ ) *Solar Optical Telescope* (SOT) on *Hinode* appear similar to coronal features. For instance, chromospheric jets have been observed in Ca II images with similar size and shapes to their coronal counterparts. The widths of the jets range between 100–400 km (Nishizuka *et al.*, 2011). Additionally, cool condensations, called coronal rain, with typical widths of 370 km (Antolin, Shibata, and Vissers, 2010) can be seen falling down magnetic-field lines at the solar limb. These condensations are thought to be the natural result of highly stratified heating in the corona. Hence, these observations indicate that a significant structure exists with a transverse size of  $\approx 300$  km. Imaging the solar corona with better than  $0.4''$  resolution then is the required next step.

In order to meet this scientific requirement, we have designed and built a narrowband EUV telescope that was flown on a NASA sounding rocket on 11 July 2012. To accomplish the required spatial resolution, the telescope had to have the highest possible throughput to achieve low exposure times and limit the effect of the rocket jitter on the spatial resolution. The characteristics of the telescope include:

- telescope design matched to  $\approx 0.1'' \text{ pixel}^{-1}$  for the solar EUV corona;
- throughput sufficient for  $< 3$ -second exposure time; and
- image-readout duration and data-storage system capable of maintaining high-cadence observations.

We explain in Section 2 our technical approach to these items. In Section 3 we describe the launch, data acquisition, and data processing. We provide an analysis of our achieved resolution in Section 4. We finally provide a summary of the first scientific results in Section 5.

## 2. Technical Approach

The Hi-C telescope design is a direct continuation of the development from the *Normal Incidence X-ray Telescope* (NIXT: Spiller *et al.*, 1991) to TRACE and AIA: we have developed a Ritchey–Chrétien telescope with plate scale sufficient to provide  $0.1''$  pixel size and a multilayer coating on the full aperture of the optics. The detector is a large-format, back-illuminated CCD, providing high quantum efficiency and rapid-readout camera electronics for high image cadence. Off-band wavelengths are eliminated by front-entrance and focal-plane filters. An H $\alpha$  telescope with NTSC (TV) output is included for real-time pointing verification during the flight.

### 2.1. Instrument Layout and Mechanical Design

The telescope is packaged inside a standard NASA “22-inch” size (approximate diameter 560 mm) rocket shell (Figure 1). The experiment section is separated by a vacuum bulkhead, with a total length of 2.766 m and total mass of 255.3 kg. The telescope section is pumped down to  $\ll 130$  Pa (or  $\ll 1$  torr) before launch to protect the thin metal filters from acoustic

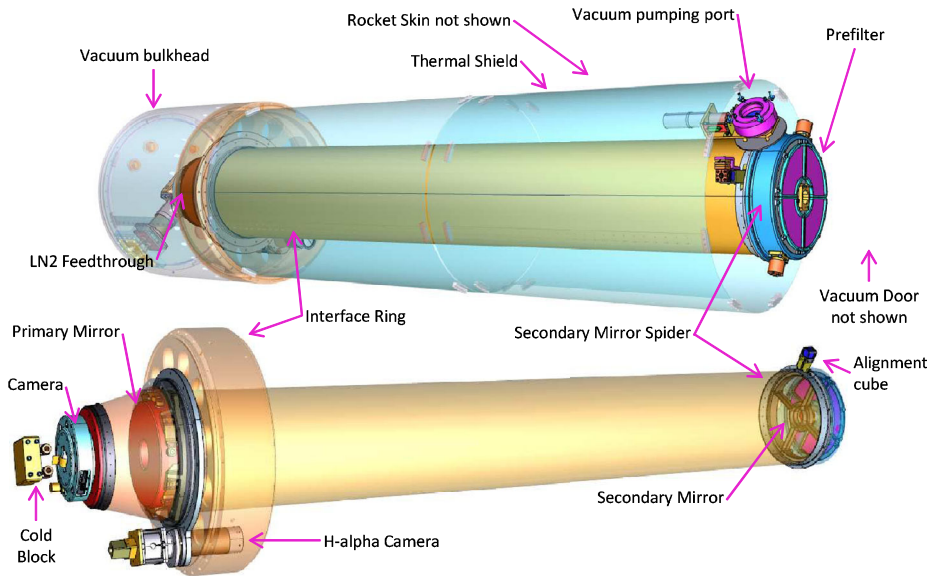


**Figure 1** The Hi-C experiment, shown without the rocket skins. The vacuum shutter door is not shown. The launch direction is to the left. The Interface Ring is  $\approx 560$  mm in diameter.

loads during flight and to prevent condensation on the cooled CCD and cold block. The experiment electronics are located outside the vacuum section to minimize outgassing in the vacuum section and to allow air cooling of the electronics until launch.

The telescope has a single mounting interface to the rocket via an interface ring, a special rocket-shell section, approximately 125 mm in length, which extends inward to provide a structurally rigid, circular mounting interface. The telescope's mounting flange, which is located at and bolted directly to the primary-mirror mount, attaches to the interface ring. The forward telescope tube, which carries the secondary-mirror spider assembly, is cantilevered from the mounting flange, as is the rear telescope tube that carries the CCD camera.

Dimensional stability of the telescope is key to maintaining alignment and achieving high resolution; thermal deformation is one of the primary concerns. Because the rocket skin heats up during ascent, two layers of thin aluminum plates are installed inside each rocket skin to act as thermal shields. The large mass of the interface ring helps minimize temperature rise during this brief period of heat input. The two parts of the telescope tube (fore and aft of the interface ring) are made of carbon-fiber-reinforced polymer, formulated for zero thermal expansion.

## 2.2. Telescope

### 2.2.1. Optical Design

The goal of Hi-C was to achieve a plate scale of  $0.1'' \text{ pixel}^{-1}$ . The Hi-C telescope specifications are shown in Table 1; it is a conventional Ritchey–Chrétien configuration, but with an extremely long focal length of 23.8 m (F/109) to achieve the  $0.1'' \text{ pixel}^{-1}$  plate scale using available CCD detectors. The primary-mirror diameter of 240 mm, with 220 mm of active area, was selected to make use of available coating facilities. The inherent aberration of

Hi-C

**Table 1** Hi-C telescope designed optical parameters.

Telescope properties		Primary Mirror	
Focal Length	23.9 m	Radius of Curvature	$4000 \pm 4.0$ mm
Plate Scale	$114 \mu\text{m arcsec}^{-1}$	Diameter	240 mm
Focal ratio	F/109	Clear Aperture	220 mm
Field of View	$7.0' \times 7.0'$	Secondary Mirror	
CCD Camera		Radius of Curvature	$370.9 \pm 0.5$ mm
Scale	$0.103'' \text{ pixel}^{-1}$	Conic	$-1.14 \pm 0.10$
Size	49.1 mm square	Diameter	30 mm

this design is under  $0.07''$  throughout the field of view, so the actual performance is limited only by optical figure of the optics and alignment accuracy. The telescope assembly was designed, built, and aligned by the Smithsonian Astrophysical Observatory.

### 2.2.2. Optics Fabrication

Mirror figure and smoothness are key factors for achieving high spatial resolution. A full description of the allocated and achieved properties of the Hi-C optical system is given by Podgorski *et al.* (2012). The mirrors were initially fabricated by the Space Optics Manufacturing Technology Center at NASA MSFC. The mirrors were polished using a conventional rotational pitch-lap process. This hand-polishing process produced a marginal primary and acceptable secondary mirror. The primary mirror was sent to Tinsley (L3 Integrated Optical Systems) for final super-polishing.

The primary and secondary mirrors were then coated with narrowband Al/Zr EUV multilayers by Reflective X-ray Optics LLC (RXO; New York, NY). These coatings, which utilize a novel aperiodic design, provide improved performance relative to the multilayers used on AIA for this wavelength, with 44 % peak reflectance at 19.3 nm and reduced out-of-band reflectance.

### 2.2.3. Telescope Assembly

In previous EUV telescopes, such as AIA, the primary mirror was bonded into cells that were then bolted to an interface. Although the bonding process introduced little stress to the mirror, bolting of the mirror cell to the telescope structure introduced distortion that would be unacceptable for Hi-C. Also, the Hi-C mirror mount was designed with six bonding pads on six flexures to cope with the large acceleration load and vibrations of a sounding-rocket launch.

We therefore decided to first bolt the telescope structure to the rocket interface ring and one of the rocket-skin sections, then bolt the mirror mount to the telescope structure, and finally bond the mirror into the mount. Furthermore, to minimize stress during bonding, it was done with the mirror in a horizontal orientation (*i.e.* telescope vertical). Details of the process, including interferometric measurements of the mounted mirror, are reported by Podgorski *et al.* (2012). Similarly, the secondary mirror was bonded into its cell with the cell pre-attached to the secondary spider, a procedure that eliminates strains due to bolting the cell to the spider. This spider/secondary-cell assembly was then bolted to the telescope front flange during telescope alignment.

#### 2.2.4. Focus and Alignment

Telescope alignment was one of the biggest challenges of Hi-C. This is partly due to the tight tolerances (see Podgorski *et al.*, 2012), but also due to the fact that Hi-C's spatial resolution is designed to be significantly better than the diffraction limit in visible light. This means the optical alignment and focus cannot be verified by testing it in visible light. The resolution requirement also means use of existing vacuum beamlines such as the MSFC X-ray Calibration Facility were impractical; the finite conjugate correction for a 23.4-m focal-length telescope would be over one meter. The extremely slow F-number leads to a large depth of focus ( $\approx 1$  mm) for the CCD, but the tolerance for the inter-optic spacing between the primary and secondary mirrors is significantly tighter ( $\approx 20$   $\mu\text{m}$ ).

The Hi-C telescope was aligned using a double-pass interferometric technique similar to that used to align the AIA telescopes. This technique uses a Zygo interferometer, equipped with a transmission sphere, placed on a five-axis mount behind the telescope focus. The interferometer is first positioned so that the converging beam from the transmission sphere is focused at the desired focus point of the telescope, by using a precision mounted reflective sphere ("retro-ball") placed at the intended focal point. The retro-ball is then removed, which allows the ZYGO beam to be reflected through the telescope and emerge as a collimated beam. A precision optical flat reflects the beam back through the telescope to the interferometer. The tip-tilt angle of the entire secondary-mirror spider assembly was adjusted using shims to optimize alignment, then the shims were replaced by machined spacers. This double-pass configuration also allowed precise measurement of focal position by measuring the power in the interferometer measurement. The focus measurement is highly sensitive to any curvature (power) of the optical flat. We used an optical flat that was independently verified to be  $\lambda/40$ .

The camera's focal-plane position relative to its flange was measured separately by focusing an optical microscope on the flange surface and then the CCD, and measuring the position shift using a coordinate-measuring machine (CMM). An adapter flange was machined to place the CCD focal plane in the same position as the center of the retro-ball, transferring the interferometric focus to the CCD.

#### 2.2.5. Filters

Like AIA, Hi-C uses two sets of filters. The front-aperture filter was made in cooperation between the Lebedev Physical Institute and the Institute for Physics of Microstructures (Russia). The filter consisted of multiple layers of Al/Si with total thickness 2.85 nm of Al and 2.05 nm of Si; the layered structure was chosen to improve mechanical strength. The filter was fixed on 0.5 mm thickness support grid with 5-mm spacing. The transmittance of the filter at 17.1 nm was about 43 %.

The focal-plane filter was a 144.2-nm Al filter, supported by a 98 % transmitting nickel mesh with 5.08-mm pitch fabricated by the Luxel Corporation. The extremely slow focal ratio of the telescope meant the shadowing effect of the filter mesh could not be avoided, but its effect is minimized through use of this thin-wire mesh and by separating the filter from the image plane as far as was practical. Each mesh wire cast a  $\approx 0.5$  mm wide shadow with up to 35 % reduction in flux, which is corrected through post-flight flatfield correction. The transmissions of filter samples were tested at NASA MSFC using discrete emission lines from a windowless EUV discharge lamp (Figure 2). While the discrepancy between the predicted and measured transmission was not fully investigated, it is believed to be due to the discrepancy between specified and actual filter thickness.

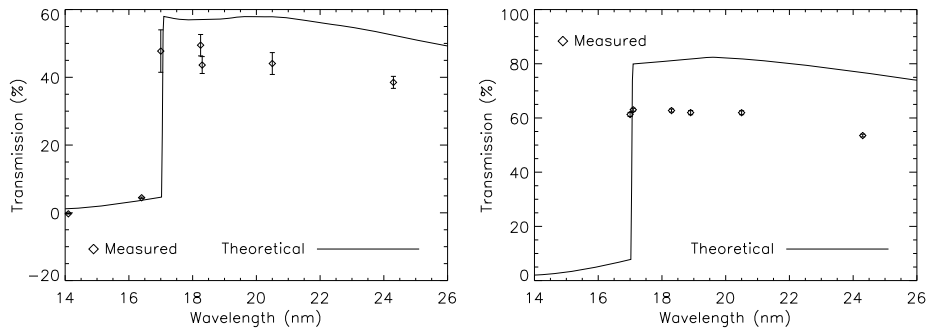


**Figure 2** Transmission of the front-aperture filter (left) and focal-plane filter (right). Solid lines show calculated transmission from nominal specifications, and data points show values measured from sample filters at MSFC.

Because of the delicate nature of these filters, it was decided that the filter samples would be vibration-tested separately, well in advance of the launch. The filter samples were mounted inside a custom-built vacuum enclosure and vibrated to the component qualification level, and no tears or pinholes were detected. The flight filters were made by the same suppliers with the same fabrication method, and they were installed after the vehicle vibration test to minimize the chance of breakage due to handling errors.

### 2.2.6. Camera

The Hi-C camera was designed and built around a customized version of the e2v CCD203-82 back-illuminated  $4096 \times 4096$  with  $13.5 \mu\text{m}$  pixel size. This device, a flight spare for AIA, has lower operating voltages than the standard CCD203-82.

The camera electronics and hardware were designed and fabricated by Apogee Imaging Systems. The camera is capable of simultaneous four-channel readout at  $2.0 \text{ megapixel s}^{-1} \text{ channel}^{-1}$ , with each channel reading one quadrant of the detector. The camera connects to the host computer through a USB 2.0 port. Due to onboard-memory constraints, only the center 3880 rows were stored and read out.

Due to schedule constraints, quantitative gain measurement and adjustment were not made before flight; the gain was set so that the CCD saturated close to but under the full range of the 16-bit A/D converter. The numerical value of the gain and readout noise were measured post-flight using a  $^{55}\text{Fe}$  radioactive source. The gain was found to be  $4.3 e^- \text{ DN}^{-1}$ . The noise was found to be markedly different for each quadrant, with  $77 e^-$  rms in the best quadrant and  $102 e^-$  rms in the worst quadrant (Table 2). These high noise values are attributed to the camera electronics, which, due to time constraints, could not be refined to reduce the noise levels.

The CCD carrier is designed for conductive cooling through a cold strap. In Hi-C, the CCD carrier is connected to a 2 kg copper thermal reservoir (cold block) located behind the camera. The cold block is connected to fluid feedthroughs on the rocket skin; a flow of liquid nitrogen (LN2) cools the cold block before launch. The CCD cold strap is made of 15 layers of 0.003-inch ( $\approx 80 \mu\text{m}$ ) thick copper; the number of necessary layers for flight was determined through laboratory testing. The flow of LN2 into the payload was controlled automatically by a ground-support equipment (GSE) computer that monitored the CCD and cold-block temperatures to ensure adequate and safe ramp rate to bring the CCD temperature below  $-50 \text{ }^\circ\text{C}$  (target  $-60 \text{ }^\circ\text{C}$ ) at launch. At the moment of launch, the cold block was at

–140 °C and the CCD at –58 °C. Over the course of ascent and observation, the cold-block temperature rose to –128 °C. Because the CCD temperature had not fully equilibrated with the cold block at time of launch, it cooled down slightly further and was at –59 °C at the end of observations.

### 2.3. Electronics

Hi-C's Data Acquisition and Control System (DACS) controls camera operations and performs data collection, processing and transmission. The DACS is an x86 architecture computer running Linux. The hardware consists of a CompactPCI backplane, a conduction-cooled single-board computer (GE Intelligent Platforms CR5), digital I/O board, a solid-state storage card, and a power supply; these components are packaged in a custom-designed chassis. The digital I/O board, custom-designed at MSFC, contains a parallel interface that is used to send formatted image data to the 10 Mbps telemetry system.

A command uplink capability was included, but only for redundancy; the DACS flight software is designed to operate without need for any uplink. Timer commands are used to initiate changes in operating mode, from standby to dark-frame acquisition, observation, and shutdown. Additional uplink commands allow for exposure-time changes, in case the downlinked images show saturation or severe under-exposure. None of the uplink commands were needed in the 2012 flight.

The DACS and flight camera are capable of a sustained 5.5-second cadence with a 2.0-second exposure time for full-frame images. The full-resolution images are saved as individual files in the standard FITS format, on a solid-state memory card with a standard FAT file system. The images are also resampled to a 1024 × 1024 and downlinked for real-time display, used to confirm instrument pointing and to assess exposure time.

A requirement unique to Hi-C was to monitor the internal vacuum and operate the vacuum valve during the flight, and also during the countdown phase before the DACS is powered on. The vacuum valve is opened just before the main telescope door, to equalize pressure and minimize the chance of the front-aperture filter blowing out when the main telescope door is used. The DACS is turned on only  $\approx$  ten minutes before flight because of over-heating concerns, and therefore the vacuum valve and vacuum gauge must be operable without the DACS. This was solved by using RS-485 interfaces that can be put into a three-state mode; both the DACS and the GSE computer can take control of the vacuum-valve controller and vacuum gauge.

### 2.4. Pointing System

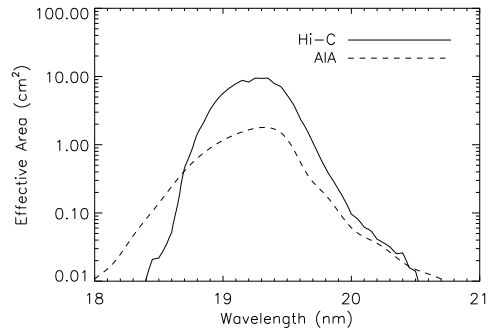
The pointing camera system is an NTSC analog video camera mounted to a 712 mm focal-length telephoto lens and an H $\alpha$  filter system, consisting of an energy rejection filter and a temperature-controlled etalon with 0.06-nm FWHM passband. This imaging system has a full-Sun field of view.

In actual flight, heating from full sunlight under vacuum created enough additional heating in the etalon that the temperature control did not converge, and on-band H $\alpha$  images were not taken. Nevertheless it provided a continuum image of the sunspot in the target active region, which was successfully used to point the experiment.

### 2.5. Radiometry

The expected Hi-C throughput was calculated from component measurements. The multilayer-mirror reflectivity was measured by RXO. The transmission of filter samples

**Figure 3** Effective area of Hi-C based on measured values of filter transmission, multilayer coating reflectivity, and CCD QE. The effective area of the AIA 19.3-nm channel is shown for reference.



were measured at NASA MSFC (see Section 2.2.5). The CCD QE curve was measured as part of the SDO/AIA program. The combined effective area curve is shown in Figure 3. Post-flight analysis using AIA 19.3-nm images as a reference indicates that, assuming the published AIA effective areas are correct, the Hi-C effective area is  $\approx 40\%$  lower than the value calculated from individual component measurements. The cause is suspected to be contamination of optical surfaces, as spacecraft-level contamination control could not be followed during integration and final testing of Hi-C. Note that this correction to the Hi-C effective area is only a rough estimate. To calculate it, we have assumed that the passbands are identical, while, in reality, the Hi-C passband has significantly less throughput in the 18.0–18.5-nm range.

### 3. Hi-C Rocket Flight, Data Acquisition and Data Processing

In this section, we describe the Hi-C launch, as well as the data acquisition and processing. Table 2 summarizes the properties of the data; these values are presented in more detail below.

Hi-C was launched at 18:50 UT, 11 July 2012 from White Sands Missile Range. The target of observation was Active Region 11520 centered at approximately  $(-130'', -453'')$  from Sun center. Table 3 provides the timeline of the Hi-C rocket flight. There were two corrections to the initial pointing obtained by the onboard Solar Pointing And Roll Control System (SPARCS). The first was just after fine pointing mode was obtained; the second was at 18:52:04, about 138 seconds into data acquisition. During the first 206 seconds of data acquisition, Hi-C recorded full detector ( $4k \times 4k$ ) images with a 2-second exposure and 5.5-second cadence. The remaining portion of the flight, Hi-C recorded the central  $1k \times 1k$  region of the detector with a 0.5-second exposure and 1.4-second cadence. Figure 4 provides the height of the sounding rocket as a function of time determined from White Sands Missile Range radar measurements. The events given in Table 3 and the approximate height at which they occurred are shown in this figure.

Comparisons with simultaneous AIA 19.3-nm images show that Hi-C is rolled  $-1.8^\circ$  from solar North; this is within the tolerances for SPARCS pointing. Figure 5 shows the full-disk AIA 19.3-nm image rotated by  $-1.8^\circ$ . The Hi-C FOV before (solid line) and after (dashed line) the observer repoint is shown. Additionally, the  $1k \times 1k$  sub-region is shown with a dash-dot line. There was an additional pointing drift throughout the flight that is not shown in this figure. The images were initially co-aligned and de-jittered by finding the offset that maximized the inter-image-correlation function, and applying optimized resampling (DeForest, 2004) to co-align adjacent frames to fixed absolute pointing. Additional

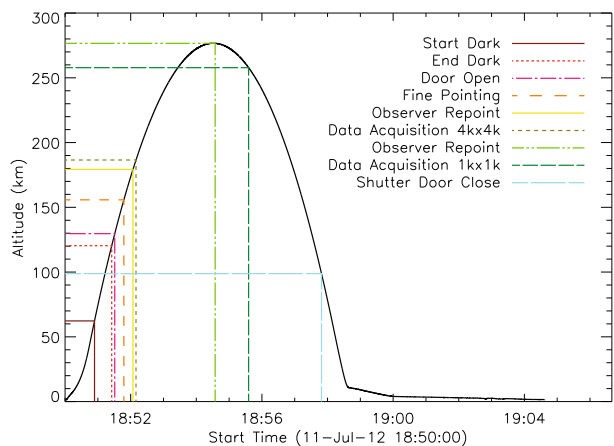
**Table 2** Hi-C data properties.

Channel	19.3 nm	Maximum Image Size	3880 × 4096
Launch Date	11 July 2012	Field of View	6.66' × 7.03'
Data Acquisition Time	18:52:10 – 18:57:49	Approximate Pointing	(−130'', −453'')
Camera Gain	4.3 e <sup>−</sup> DN <sup>−1</sup>	Roll	−1.8°
Camera Noise:		4k × 4k Data Set:	
NE Quad	24.4 DN	Exposure time	2 s
NW Quad	19.4 DN	Cadence	5.5 s
SE Quad	36.4 DN	No. of Images	36
SW Quad	16.0 DN	1k × 1k Data Set:	
Plate Scale	0.103'' pixel <sup>−1</sup>	Exposure time	0.5 s
Avg. Spatial Resolution	0.3''	Cadence	1.4 s
		No. of Images	86

**Table 3** Hi-C timeline.

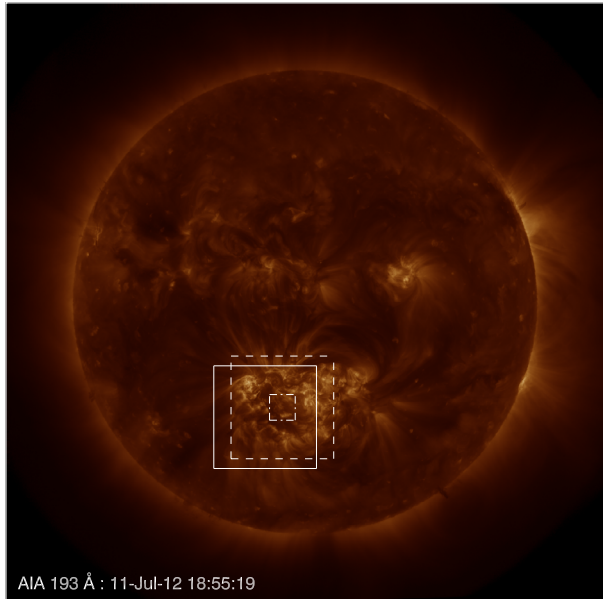
Event	Time
Launch	18:50:00
Start Dark Exposures	18:50:54
End Dark Exposures	18:51:25
Shutter Door Open	18:51:31
Fine Pointing	18:51:48
Observer Repoint	18:52:04
Data Acquisition (4k × 4k)	18:52:10
Observer Repoint	18:54:34
Data Acquisition (1k × 1k)	18:55:36
Shutter door close	18:57:49

**Figure 4** The altitude of the Hi-C rocket as a function of time determined from White Sands Missile Range radar data. The events given in Table 3 are shown.



fine co-alignment shifts to the pointing were determined manually. Absolute pointing was determined by comparing to co-temporal AIA images and calculating the drift. The headers

**Figure 5** The AIA 19.3-nm data taken at 18:55:19 rotated by  $-1.8^\circ$ . The initial Hi-C field of view is shown with a solid line, the field of view after the repoint is shown as a dashed line. The  $1\text{k} \times 1\text{k}$  field of view is shown as a dashed-dot line. The pointing also drifted during flight, this information is not captured in these images.



of the data files were adjusted to include the best approximation of the absolute pointing of the instrument at the time of the data file.

The time on the Hi-C onboard computer slowly drifts, implying the onboard time was many seconds different from true time at launch. When launch occurred, the computer recorded the onboard time of the event. After flight, this was compared to the actual launch time. The difference, 92 seconds, was then applied to the header of all data files.

During ascent, Hi-C obtained five dark frames. The median value was found for each pixel of the dark frames; this image, shown in the upper left of Figure 6, was used as the dark image for all data processing. The raw data were further degraded by the shadow of the mesh of the focal-plane filter, reducing the intensity behind the mesh by  $\approx 35\%$ . The data were divided by the flatfield to remove the shadow. The flatfield, shown in the upper-middle of Figure 6, was generated from the blurred images taken before the pointing had stabilized. While this flatfield adequately flattens the images, a few regions remain affected by the mesh due to the insufficient time to acquire a full calibration set.

Additionally, there was dust present on the detector, due in part to the repeated handling of the CCD as well as incomplete cleanliness controls during integration and testing at the launch site. Most of the dust particles were present at launch, but some dust particles were observed to appear during flight, including a few that appeared suddenly during the observing sequence. Presumably this dust originated from the telescope structure and was deposited during flight. An initial dust map was generated by applying a threshold to the Hi-C images that were blurred by the repointing procedures. The dust map is shown in the upper right of Figure 6. A second dust map was created by applying a thresholding technique to the images in which new dust appeared suddenly during the acquisition of the  $1\text{k} \times 1\text{k}$  image sequence. To correct for dust, the intensity in pixels identified in the dust map was interpolated from the nearest pixels not containing dust. The lower left of Figure 6 shows the raw Hi-C data; the lower-right panel in Figure 6 shows the dark-subtracted, flatfielded, and dust-corrected image.

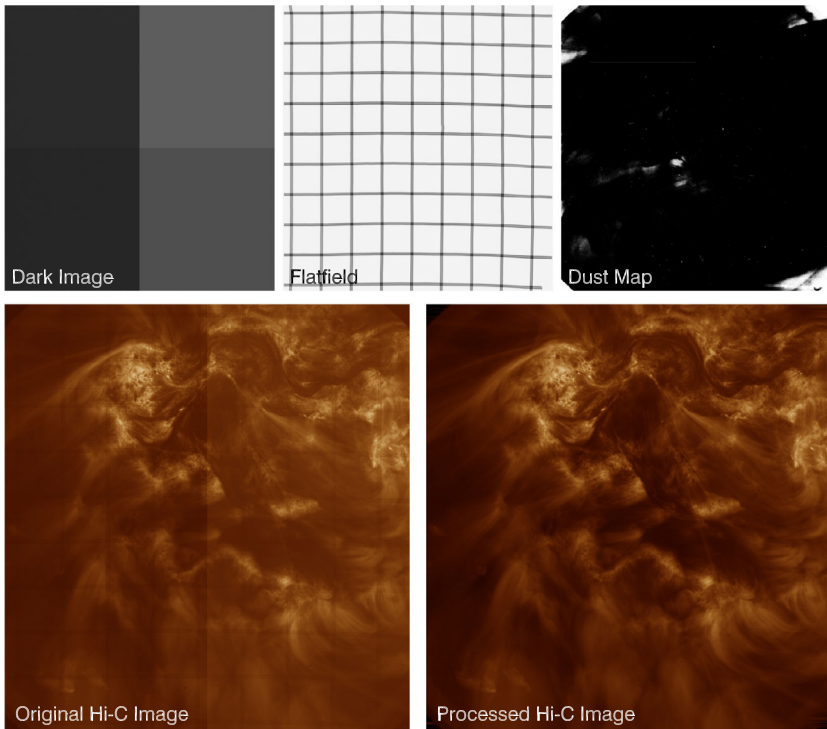


**Figure 6** The upper panels show the dark image, flatfield, and dust map, respectively. The bottom-left panel shows an example of the raw Hi-C data, the lower-right panel shows a processed image. Each image is  $6.66' \times 7.03'$ .

The data had to be corrected in order to compensate for the two missing columns that were not read out from the CCD along the center of the raw images. To compensate for the missing data, corresponding pixels were added and set to the mean value of the immediately adjacent pixels.

While Hi-C was traveling through the atmosphere, the degree of atmospheric absorption in the 19.3-nm wavelength range varied. We use the flight data to assess the atmospheric absorption of the 19.3-nm signal as a function of the rocket height. The left panel of Figure 7 shows the total intensity in the aligned  $1\text{k} \times 1\text{k}$  field of view as a function of time. We average the intensities during the time the rocket is near its peak; this average value is shown as a horizontal dashed line. We then find the ratio of the observed intensity (solid line) to the average peak intensity (dashed line) as a function of height. This ratio is shown in the right panel of Figure 7. This demonstrates that the 19.3-nm signal falls by roughly 50% at 150 km.

The science team has generated several different data sets for community-wide distribution, as well as a software package to prepare and analyze the early-release data. The levels of the data are described in Table 4. Level-0.5 data was generated by transposing the raw data (to put solar North in the  $+y$ -direction of the image), compensating for the missing center rows, and correcting the FITS file header for time and pointing. Level-1.0 data are dark-subtracted, flatfielded, dust-corrected, and cropped to remove extraneous columns. Level-1.5 data are co-aligned with tracking to remove the pointing drift, repoint, and jitter

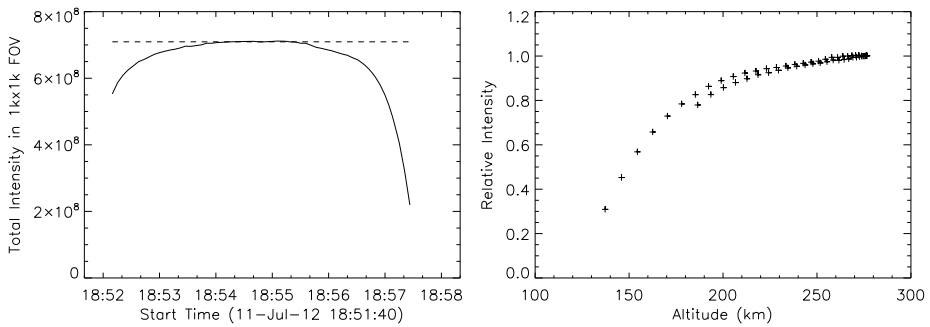


**Figure 7** Left Panel: The intensity summed in the  $1\text{k} \times 1\text{k}$  field of view is shown with a solid line. The average intensity near the peak of the curve is shown with a dashed line. Right Panel: The ratio between the observed intensity and the expected (average peak) intensity as a function of altitude. At 150 km, the atmosphere absorbed roughly 50 % of the 19.3-nm signal.

**Table 4** Levels of Hi-C data sets.

Level	Description
0.5	Transposed the raw data Compensated for the missing center rows Corrected the FITS file header for time and pointing
1.0	Dark-subtracted, flatfielded, dust-corrected, cropped
1.5	Co-aligned, normalized, and corrected for atmospheric absorption ( $1\text{k} \times 1\text{k}$ only) Relevant region included from $4\text{k} \times 4\text{k}$ data set
1.5 stacked	( $1\text{k} \times 1\text{k}$ only) four $1\text{k} \times 1\text{k}$ images are combined to effectively generate data at the same exposure time and cadence as the $4\text{k} \times 4\text{k}$ data set
2.0	( $1\text{k} \times 1\text{k}$ only) Scaling applied to Level-1.5 data to generate smooth transitions between quadrants and noise is suppressed. This data set is useful for qualitative analysis only
2.0 stacked	( $1\text{k} \times 1\text{k}$ only) Same as Level 2.0 but with stacked data

in the images. Level-1.5 data have also been normalized for the exposure time and corrected for atmospheric absorption.

The  $1\text{k} \times 1\text{k}$  images were similarly processed into Level-0.5, Level-1.0, and Level-1.5 data sets. For the Level-1.0 set, appropriate dark, flatfield, and dust-map images were extracted from the original  $4\text{k} \times 4\text{k}$  calibration files to match the  $1\text{k} \times 1\text{k}$  field of view on the detector. The second dust map was also applied to correct for the sudden appearance of additional dust starting at 18:56:14.46 UT. To make a complete, continuous image sequence over the full flight, the extracted region from the corresponding-level  $4\text{k} \times 4\text{k}$  set is included in the Level-1.5 data set. This implies that there is an exposure time and cadence shift in the Level-1.5 data; the extracted  $4\text{k} \times 4\text{k}$  data have an exposure time of 2.0 seconds and a cadence of 5.5 seconds, while the  $1\text{k} \times 1\text{k}$  data have an exposure time of 0.5 seconds and a cadence of 1.4 seconds. Hence, we additionally generate a “stacked”  $1\text{k} \times 1\text{k}$  data set which combines four high-cadence  $1\text{k} \times 1\text{k}$  images into a single image by taking the mean value of each pixel. The result is a data set with similar exposure time and cadence throughout.

The short exposure time of the  $1\text{k} \times 1\text{k}$  data set results in low signal-to-noise output. Additionally, the effect of the readout noise, which varies by quadrant, becomes particularly prevalent. Therefore, we applied additional processing to generate a Level-2 data set for the

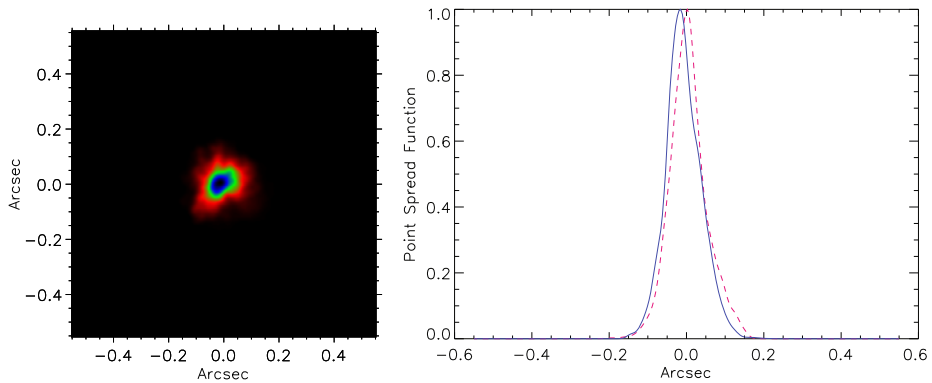


**Figure 8** Left panel: The expected two-dimensional Hi-C PSF computed using pre-flight mirror surface figure and alignment test data. Right panel: The  $x$  (solid line) and  $y$  (dashed line) one-dimensional slices through the PSF, indicating a FWHM of less than  $0.1''$ .

$1\text{k} \times 1\text{k}$  region only. In this data set, the quadrants are scaled to generate smooth transitions between adjacent quadrants and additional scalings are applied to generate smoothed transitions between subsequent images. The result is a qualitative data set only; this data set is particularly useful for generating movies of the  $1\text{k} \times 1\text{k}$  region.

There have been several releases of the data by the science team via the Virtual Solar Observatory (VSO: Hill *et al.*, 2009). The software package for processing the early distribution is available through SolarSoft (Freeland and Handy, 1998). Information on the data releases and image processing is available in a user guide distributed with the VSO package or on the Hi-C website ([hic.msfc.nasa.gov](http://hic.msfc.nasa.gov)).

#### 4. Hi-C Resolution

The primary goal of the Hi-C mission was to take high-resolution images of the solar corona. The expected Hi-C point-spread function (PSF) was computed using pre-flight mirror surface figure and alignment test data. Interferometer tests were performed on the mounted primary and secondary mirrors. These data were combined with the telescope alignment data in a Zemax ray trace, and the two-dimensional PSF, shown in the left panel of Figure 8, was computed. One-dimensional slices through the PSF, shown in the right panel of Figure 8, indicate a FWHM of less than  $0.1''$ . The predicted RMS diameter, however, was found to be  $0.4''$  (see Podgorski *et al.*, 2012). This discrepancy is due to a non-Gaussian PSF, which has a narrow peak, but it spreads beyond an equivalent Gaussian below the half-maximum value. This is the result of both the telescope surface finish and the mirror mounting. The resolution of high-contrast features is predicted more accurately by the FWHM, than by the RMS, as shown below in an analysis of the images themselves.

The resolution of the images is a result of both the PSF of the optics and the stability of the pointing control of the rocket. One method of determining the width of the point-spread function from the flight data is to simply look for the fine-scale structure in the corona. Figure 9 shows some comparisons of structures observed with AIA 19.3 nm (left column) and Hi-C (middle column). Care has been taken to scale the image pairs similarly, although the different regions have different scaling. A line is shown on each pair of images. The

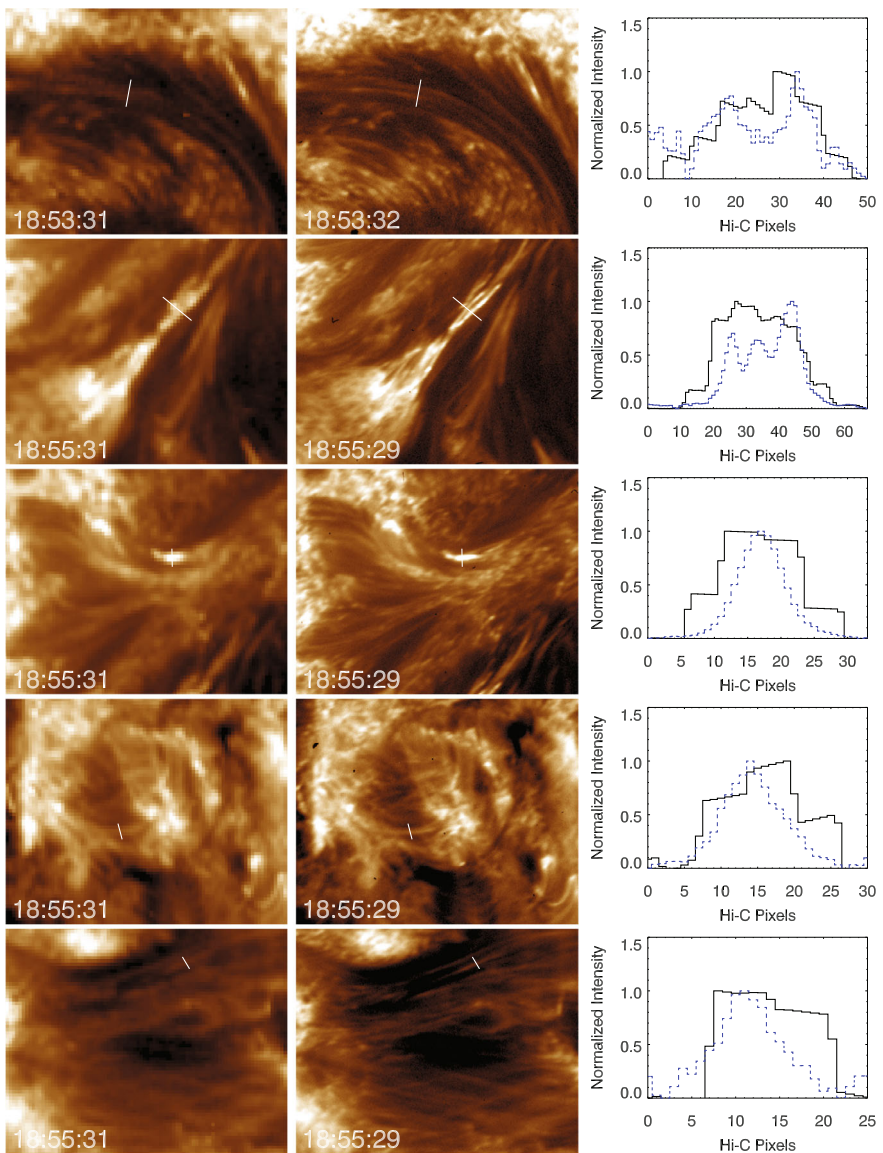
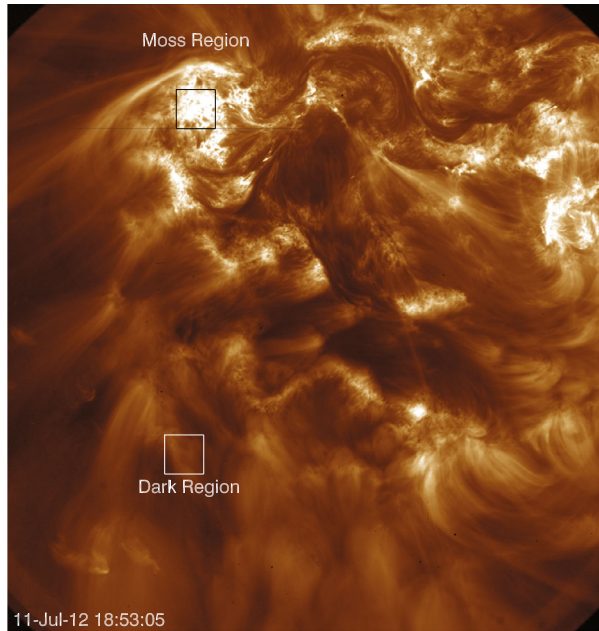


**Figure 9** Left Column: AIA 19.3-nm images. Middle Column: Hi-C images. The intensity along the line in each image pair is shown in the right column. The dashed line is Hi-C; the solid line is AIA.

intensity in the AIA 19.3-nm image and the Hi-C image along the line is shown in the right column. A constant background has been subtracted from the intensities, and they have been normalized.

The top two rows of Figure 9 show examples of Hi-C resolving substructure in what appear to be single, broad AIA structures. In the top row, Hi-C resolves two unique structures, in the second row, Hi-C resolves three unique structures. In the lower three panels, both instruments appear to image single structures, the width of the structures in Hi-C is smaller

**Figure 10** The full Hi-C image ( $6.66' \times 7.03'$ ) taken at 18:53:05. The smaller regions, labeled Moss and Dark, along with the entire image were used for Fourier analysis.



than the width of the structures in AIA. This reduction in width is attributed to the smaller PSF of Hi-C.

In addition to identifying the smallest possible features, we analyzed the Hi-C spatial resolution via Fourier analysis. The first five or six frames after each pointing command show an anisotropic blur, which we attribute to settling of the SPARCS system; the first clear frame was taken at 18:53:05, which is shown in Figure 10. For the first pointing sequence, 16 frames show clear steady pointing with frame-to-frame drift of order one or two pixels. We apodized and Fourier transformed the first frame at 18:53:05 and two of its sub-regions, averaged over azimuth, and extracted the absolute amplitude of each spatial frequency component to generate a spatial spectrum reported by the instrument. The left panel of Figure 11 is a log–log plot of such spectra for several elements of the image.

The “Full Frame” trace in the left panel of Figure 11 is the average spatial spectrum of the full-frame image. At spatial frequencies between  $0.3 \text{ arcsec}^{-1}$  and  $1 \text{ arcsec}^{-1}$ , the slope is approximately  $-2$ . The Hi-C spectrum tracks the corresponding spectrum from the simultaneous AIA 19.3-nm frame (“AIA” trace) up to the AIA Nyquist frequency of  $1.2 \text{ arcsec}^{-1}$  (the AIA 19.3-nm amplitudes have been multiplied by five to scale them to the Hi-C pixel values). At higher spatial frequencies there is a break in the Hi-C spectrum, which we attribute to noise in the Hi-C image. This attribution is supported by the “Moss Region” and “Dark Region” lines, which are spectra of bright and faint regions of the image, respectively. The break in the spatial spectrum shifts from  $1.4 \text{ arcsec}^{-1}$  to  $0.7 \text{ arcsec}^{-1}$  in these two sub-regions. The “Dark Image” trace is a similar spectrum of a dark portion of the Hi-C image, showing the white nature of the detector noise: it agrees well with the noise portion of the faint region from the image. We attribute the varying noise levels to photon noise in the individual images.

To further understand the spectrum and verify that the high-frequency spectrum is formed by photon noise, we smoothed across several images to generate a lower-noise spectrum. The images were co-aligned *a posteriori*: by correlation and optimized resampling. The

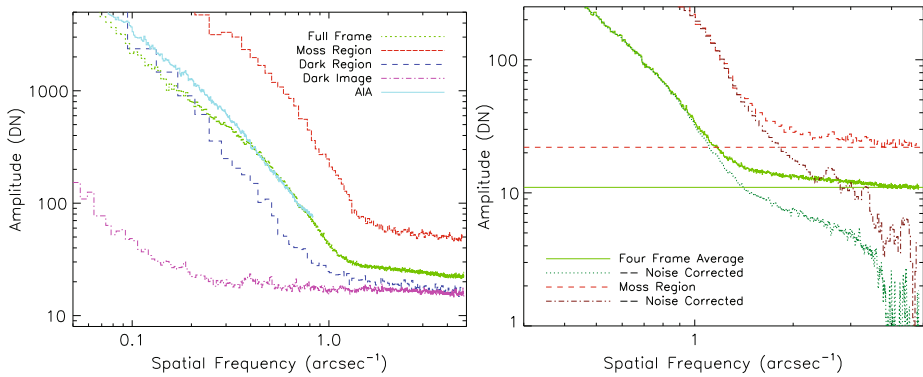


**Figure 11** Fourier analysis of AIA and Hi-C images reveals Hi-C’s resolution. Left panel: Hi-C agrees well with AIA at spatial frequencies below  $1 \text{ arcsec}^{-1}$ ; the spectral break at  $1\text{--}1.5 \text{ arcsec}^{-1}$  is due to noise effects and shifts in the bright moss region. Right panel: Subtracting the measured noise amplitude in quadrature softens the spectral break and reveals that solar structure is detected in bright moss at frequencies above  $3 \text{ arcsec}^{-1}$  ( $0.3''$  resolution).

Hanning window used for resampling the images attenuated the very highest spatial frequencies slightly, and we corrected for this by normalizing the spectrum of a single resampled image to that of the same frame before resampling. In averages across these co-aligned images, the high spatial frequencies behave as one would expect for uncorrelated noise. The right panel of Figure 11 shows spectra of the full-frame and moss regions, averaged across four exposures. The spectra maintain their shape but the noise floor is a factor of 2.0 lower, as expected for an incoherent average of four noise samples. Photon noise, if truly uncorrelated, should yield a nearly flat spectrum, and we have marked the expected shape of that spectrum with horizontal lines. The actual solar image spectra are tilted, and we attribute this tilt to a combination of image correlation of the photon noise and the image itself.

Removing the fixed component of the noise using subtraction in quadrature yields a better estimate of the solar signal underlying the spectrum. The “Dark Image” and “Full Frame” traces in the left panel of Figure 11 show the result of subtracting the marked fixed components of the corresponding spectra. While the full-frame average spectrum breaks to a slightly steeper slope, the bright moss region (with its lower relative contribution of photon noise) maintains a slope close to that of the AIA-compatible range. We conclude that there is significant coherent solar signal contained in the Hi-C bright images up to at least spatial frequencies of  $3\text{--}4 \text{ arcsec}^{-1}$  based on analysis of the spatial Fourier spectrum, quite close to the spatial Nyquist frequency of  $5 \text{ arcsec}^{-1}$ .

## 5. Conclusions

The Hi-C instrument was built to resolve small-scale structures in the solar corona with the highest resolution of any previous coronal imager. In this article, we have presented the details of the Hi-C instrument, rocket flight, data acquisition, data processing, and image resolution. There have already been several scientific studies completed on this very short data set.

The most significant result of the Hi-C mission is the confirmation of Parker-like braiding in the solar corona (Cirtain *et al.*, 2013). There are two clear examples of braiding in the Hi-C

region, and both are associated with small flares that occur before or after the Hi-C flight. Cirtain *et al.* (2013) estimated the magnetic energy contained in one of these structures using the local magnetic-field strengths and determined that only 1 % of the magnetic free energy was expended during the reconnection event. Thalmann, Tiwari, and Wiegelmann (2014) use non-linear force-free magnetic-field extrapolations to confirm the presence of magnetic-field braiding with one of the structures. They provide an updated estimate of the magnetic free energy from the vector field and find it to be two orders of magnitude larger than the estimate by Cirtain *et al.* (2013).

Dissipation of Alfvén waves has long been proposed as a candidate mechanism for coronal heating, but determining the wave amplitude *versus* wave period for input into theoretical models has been severely limited by the spatial resolution and cadence of EUV imagers. The improved resolution of Hi-C allowed for the measurement of Alfvénic motions in the Hi-C data; the results provide tantalizing evidence of short-period waves below the current error estimates obtained with AIA (Morton and McLaughlin, 2013).

One objective of Hi-C was to study the substructure of the coronal features observed in  $> 1''$  imagers, such as AIA. Hi-C has revealed that some AIA structures appear to be a single structure in Hi-C (for instance, the bottom three panels in Figure 9). If this singular structure were indeed a collection of strands, Peter *et al.* (2013) calculated the diameter of the strands would have to be less than 15 km. Brooks *et al.* (2013) found several examples of a single AIA structure that were composed of multiple Hi-C structures (for instance, see the top two panels of Figure 9). They found the most frequent width of the Hi-C structures was 270 km.

There have been two solar features that were discovered in the Hi-C data that have never been seen before in EUV images. Alexander *et al.* (2013) discovered counter-streaming flows along a complex solar filament; the velocities of the flows range from  $70 - 100 \text{ km s}^{-1}$ . Such flows are commonly seen in H $\alpha$ . Régnier *et al.* (2014) discovered small-scale brightenings in the northeast corner of the Hi-C field of view with lifetimes on the order of 25 seconds. These brightenings appear to occur at the footpoints of long extended loops. In both of these examples, the features were not clearly apparent in the co-temporal AIA data. We attribute these new discoveries to both the increase in spatial resolution and the rapid cadence of the Hi-C images.

Finally, the high-resolution images, coupled with the high-cadence capability of the telescope, allowed Hi-C to probe the prevalence of short heating events, potentially related to nanoflare production, in the solar corona. Testa *et al.* (2013) studied the small-scale dynamics observed in a small region of moss in the Hi-C data. They found the moss at the footpoints of high-temperature ( $\approx 8 \text{ MK}$ ) loops demonstrated short-lived ( $\approx 15$  seconds) brightenings, while other moss patches not associated with such high-temperature structures were more steady. Winebarger *et al.* (2013) studied transient events between two regions of moss and found they were likely cool, transition region loops caused by low-lying nanoflares.

The scientific objectives of Hi-C are central to the goal of understanding the Sun's activity and its effects on the terrestrial environment by providing unprecedented views of the dynamic activity in the hot, magnetized solar atmosphere. Hi-C has served as a path-finder for a future NASA mission in that it set an upper limit to the size of heating and cooling elementary threads, and it explored the temperature range in which they can be observed.

**Acknowledgements** We acknowledge the High-Resolution Coronal Imager instrument grant funded by the NASA's Low Cost Access to Space program. MSFC/NASA led the mission and partners include the Smithsonian Astrophysical Observatory in Cambridge, MA, USA; Lockheed Martin's Solar Astrophysical Laboratory in Palo Alto, CA, USA; the University of Central Lancashire in Lancashire, England; and the Lebedev Physical Institute of the Russian Academy of Sciences in Moscow, Russia. LPI was supported by the Program no. 22 of the Presidium of the RAS.

## References

- Alexander, C.E., Walsh, R.W., Régnier, S., Cirtain, J., Winebarger, A.R., Golub, L., Kobayashi, K., Platt, S., Mitchell, N., Korreck, K., DePontieu, B., DeForest, C., Weber, M., Title, A., Kuzin, S.: 2013, Antiparallel EUV flows observed along active region filament threads with Hi-C. *Astrophys. J. Lett.* **775**, L32. DOI. ADS.
- Antolin, P., Shibata, K., Vissers, G.: 2010, Coronal rain as a marker for coronal heating mechanisms. *Astrophys. J.* **716**, 154. DOI. ADS.
- Brooks, D.H., Warren, H.P., Ugarte-Urra, I.: 2012, Solar coronal loops resolved by Hinode and the Solar Dynamics Observatory. *Astrophys. J. Lett.* **755**, L33. DOI. ADS.
- Brooks, D.H., Warren, H.P., Ugarte-Urra, I., Winebarger, A.R.: 2013, High spatial resolution observations of loops in the solar corona. *Astrophys. J. Lett.* **772**, L19. DOI. ADS.
- Cirtain, J.W., Golub, L., Winebarger, A.R., de Pontieu, B., Kobayashi, K., Moore, R.L., Walsh, R.W., Korreck, K.E., Weber, M., McCauley, P., Title, A., Kuzin, S., DeForest, C.E.: 2013, Energy release in the solar corona from spatially resolved magnetic braids. *Nature* **493**, 501. DOI. ADS.
- DeForest, C.E.: 2004, On re-sampling of solar images. *Solar Phys.* **219**, 3. DOI. ADS.
- Delaboudinière, J.-P., Artzner, G.E., Brunaud, J., Gabriel, A.H., Hochedez, J.F., Millier, F., Song, X.Y., Au, B., Dere, K.P., Howard, R.A., Kreplin, R., Michels, D.J., Moses, J.D., Defise, J.M., Jamar, C., Rochus, P., Chauvineau, J.P., Marioge, J.P., Catura, R.C., Lemen, J.R., Shing, L., Stern, R.A., Gurman, J.B., Neupert, W.M., Maucherat, A., Clette, F., Cugnon, P., van Dessel, E.L.: 1995, EIT: Extreme-Ultraviolet Imaging Telescope for the SOHO mission. *Solar Phys.* **162**, 291. DOI. ADS.
- Démoulin, P.: 2005, Magnetic topologies: where will reconnection occur? In: Innes, D.E., Lagg, A., Solanki, S.A. (eds.) *Chromospheric and Coronal Magnetic Fields SP-596*, ESA, Noordwijk. ADS.
- Freeland, S.L., Handy, B.N.: 1998, Data analysis with the SolarSoft system. *Solar Phys.* **182**, 497. DOI. ADS.
- Handy, B.N., Acton, L.W., Kankelborg, C.C., Wolfson, C.J., Akin, D.J., Bruner, M.E., Carvalho, R., Catura, R.C., Chevalier, R., Duncan, D.W., Edwards, C.G., Feinstein, C.N., Freeland, S.L., Friedlaender, F.M., Hoffmann, C.H., Hurlburt, N.E., Jurcevich, B.K., Katz, N.L., Kelly, G.A., Lemen, J.R., Levay, M., Lindgren, R.W., Mathur, D.P., Meyer, S.B., Morrison, S.J., Morrison, M.D., Nightingale, R.W., Pope, T.P., Rehse, R.A., Schrijver, C.J., Shine, R.A., Shing, L., Strong, K.T., Tarbell, T.D., Title, A.M., Torgerson, D.D., Golub, L., Bookbinder, J.A., Caldwell, D., Cheimets, P.N., Davis, W.N., Deluca, E.E., McMullen, R.A., Warren, H.P., Amato, D., Fisher, R., Maldonado, H., Parkinson, C.: 1999, The Transition Region and Coronal Explorer. *Solar Phys.* **187**, 229.
- Hill, F., Martens, P., Yoshimura, K., Gurman, J., Hourclé, J., Dimitoglou, G., Suárez-Solá, I., Wampler, S., Reardon, K., Davey, A., Bogart, R.S., Tian, K.Q.: 2009, The Virtual Solar Observatory – a resource for international heliophysics research. *Earth Moon Planets* **104**, 315. DOI. ADS.
- Lemen, J.R., Title, A.M., Akin, D.J., Boerner, P.F., Chou, C., Drake, J.F., Duncan, D.W., Edwards, C.G., Friedlaender, F.M., Heyman, G.F., Hurlburt, N.E., Katz, N.L., Kushner, G.D., Levay, M., Lindgren, R.W., Mathur, D.P., McFeaters, E.L., Mitchell, S., Rehse, R.A., Schrijver, C.J., Springer, L.A., Stern, R.A., Tarbell, T.D., Wuelser, J.-P., Wolfson, C.J., Yanari, C., Bookbinder, J.A., Cheimets, P.N., Caldwell, D., Deluca, E.E., Gates, R., Golub, L., Park, S., Podgorski, W.A., Bush, R.I., Scherrer, P.H., Gumm, M.A., Smith, P., Auker, G., Jerram, P., Pool, P., Soufli, R., Windt, D.L., Beardsley, S., Clapp, M., Lang, J., Waltham, N.: 2012, The Atmospheric Imaging Assembly (AIA) on the Solar Dynamics Observatory (SDO). *Solar Phys.* **275**, 17. DOI. ADS.
- Linton, M.G., Longcope, D.W.: 2006, A model for patchy reconnection in three dimensions. *Astrophys. J.* **642**, 1177. DOI. ADS.
- Morton, R.J., McLaughlin, J.A.: 2013, Hi-C and AIA observations of transverse magnetohydrodynamic waves in active regions. *Astron. Astrophys.* **553**, L10. DOI. ADS.
- Nishizuka, N., Nakamura, T., Kawate, T., Singh, K.A.P., Shibata, K.: 2011, Statistical study of chromospheric anemone jets observed with Hinode/SOT. *Astrophys. J.* **731**, 43. DOI. ADS.
- Parker, E.N.: 1972, Topological dissipation and the small-scale fields in turbulent gases. *Astrophys. J.* **174**, 499. DOI. ADS.
- Peter, H., Bingert, S., Klimchuk, J.A., DeForest, C., Cirtain, J.W., Golub, L., Winebarger, A.R., Kobayashi, K., Korreck, K.E.: 2013, Structure of solar coronal loops: from miniature to large-scale. *Astron. Astrophys.* **556**, A104. DOI. ADS.
- Podgorski, W.A., Caldwell, D., McCracken, K., Ordway, M.P., Cheimets, P.N., Korreck, K., Golub, L., Cirtain, J., Kobayashi, K.: 2012, Minimizing the mirror distortion for subarcsecond imaging in the Hi-C EUV telescope. In: *Proc. SPIE 8502*. DOI. ADS.
- Régnier, S., Alexander, C.E., Walsh, R.W., Winebarger, A.R., Cirtain, J., Golub, L., Korreck, K.E., Mitchell, N., Platt, S., Weber, M., De Pontieu, B., Title, A., Kobayashi, K., Kuzin, S., DeForest, C.E.: 2014, Sparkling extreme-ultraviolet bright dots observed with Hi-C. *Astrophys. J.* **784**, 134. DOI. ADS.

- Rosner, R., Tucker, W.H., Vaiana, G.S.: 1978, Dynamics of the quiescent solar corona. *Astrophys. J.* **220**, 643.
- Spiller, E., McCorkle, R.A., Wilczynski, J.S., Golub, L., Nystrom, G., Takacs, P.Z., Welch, C.: 1991, Normal-incidence soft X-ray telescopes. *Opt. Eng.* **30**, 1109. DOI. ADS.
- Testa, P., De Pontieu, B., Martínez-Sykora, J., DeLuca, E., Hansteen, V., Cirtain, J., Winebarger, A., Golub, L., Kobayashi, K., Korreck, K., Kuzin, S., Walsh, R., DeForest, C., Title, A., Weber, M.: 2013, Observing coronal nanoflares in active region moss. *Astrophys. J. Lett.* **770**, L1. DOI. ADS.
- Thalmann, J.K., Tiwari, S.K., Wiegelmann, T.: 2014, Force-free field modeling of twist and braiding-induced magnetic energy in an active-region corona. *Astrophys. J.* **780**, 102. DOI. ADS.
- Tsuneta, S.: 1996, Structure and dynamics of magnetic reconnection in a solar flare. *Astrophys. J.* **456**, 840. DOI. ADS.
- Vaiana, G.S., Davis, J.M., Giacconi, R., Krieger, A.S., Silk, J.K., Timothy, A.F., Zombeck, M.: 1973, X-ray observations of characteristic structures and time variations from the solar corona: preliminary results from SKYLAB. *Astrophys. J. Lett.* **185**, L47.
- van Ballegoijen, A.A.: 1985, Electric currents in the solar corona and the existence of magnetostatic equilibrium. *Astrophys. J.* **298**, 421. DOI. ADS.
- Warren, H.P., Winebarger, A.R., Mariska, J.T., Doschek, G.A., Hara, H.: 2008, Observation and modeling of coronal “moss” with the EUV imaging spectrometer on Hinode. *Astrophys. J.* **677**, 1395. DOI. ADS.
- Winebarger, A.R., Walsh, R.W., Moore, R., De Pontieu, B., Hansteen, V., Cirtain, J., Golub, L., Kobayashi, K., Korreck, K., DeForest, C., Weber, M., Title, A., Kuzin, S.: 2013, Detecting nanoflare heating events in subarcsecond inter-moss loops using Hi-C. *Astrophys. J.* **771**, 21. DOI. ADS.
- Zombeck, M.V., Vaiana, G.S., Haggerty, R., Krieger, A.S., Silk, J.K., Timothy, A.: 1978, An atlas of soft X-ray images of the solar corona from SKYLAB. *Astrophys. J. Suppl.* **38**, 69. DOI. ADS.